Effectivity and efficiency of selective frequency damping for the computation of unstable steady-state solutions

Casacuberta, Jordi; Groot, Koen J.; Tol, Henry J.; Hickel, Stefan

DOI
10.1016/j.jcp.2018.08.056

Publication date
2018

Document Version
Accepted author manuscript

Published in
Journal of Computational Physics

Effectivity and Efficiency of Selective Frequency Damping for the Computation of Unstable Steady-State Solutions

J. Casacuberta, K. J. Groot, H. J. Tol, S. Hickel

Aerodynamics Group, Faculty of Aerospace Engineering, Technische Universiteit Delft
Kluyverweg 1, 2629 HS Delft, The Netherlands

Abstract

Selective Frequency Damping (SFD) is a popular method for the computation of globally unstable steady-state solutions in fluid dynamics. The approach has two model parameters whose selection is generally unclear. In this article, a detailed analysis of the influence of these parameters is presented, answering several open questions with regard to the effectiveness, optimum efficiency and limitations of the method. In particular, we show that SFD is always capable of stabilising a globally unstable systems ruled by one unsteady unstable eigenmode and derive analytical formulas for optimum parameter values. We show that the numerical feasibility of the approach depends on the complex phase angle of the most unstable eigenvalue. A numerical technique for characterising the pertinent eigenmodes is presented. In combination with analytical expressions, this technique allows finding optimal parameters that minimise the spectral radius of a simulation, without having to perform an independent stability analysis. An extension to multiple unstable eigenmodes is derived. As computational example, a two-dimensional cylinder flow case is optimally stabilised using this method. We provide a physical interpretation of the stabilisation mechanism based on, but not limited to, this Navier-Stokes example.

1. Introduction

Understanding fluid flow instabilities is of fundamental importance for laminar-turbulent transition and for flow control. Flow instabilities can be characterised through linear stability analysis, for which it is necessary to obtain an accurate representation of the laminar base flow solution [1, 2]. Letting f be the non-linear Navier-Stokes operator applied to a state variables $\boldsymbol{q}$ vector, with adequate boundary and initial conditions, the Navier-Stokes equations can be written as

$$\dot{\boldsymbol{q}} = f(\boldsymbol{q}), \tag{1}$$

where the dot expresses the time derivative. The steady state of eq. (1) satisfies $\dot{\boldsymbol{q}}_{\boldsymbol{s}} = f(\boldsymbol{q}_{\boldsymbol{s}}) = 0$. The stability approach relies on decomposing the instantaneous flow field into the base flow $\boldsymbol{q}_{\boldsymbol{s}}$ plus a time-dependent infinitesimally small perturbation field $\boldsymbol{q}'$ such that

$$\boldsymbol{q}(\boldsymbol{x}, t) = \boldsymbol{q}_s(\boldsymbol{x}) + \epsilon_{\mathrm{A}} \boldsymbol{q}'(\boldsymbol{x}, t), \quad 0 < \epsilon_{\mathrm{A}} \ll 1, \tag{2}$$

where $\boldsymbol{x}$ represents the spatial coordinates and t the time [2, 3]. Stability analysis requires an accurate solution of the base flow as the stability properties critically depend on its spatial derivatives.

The difficulty in computing time-independent Navier-Stokes solutions arises for globally unstable flow fields, inasmuch as the instantaneous flow naturally diverges from the steady state [4]. To overcome this obstacle, mainly two numerical methods are employed in the literature: Newton iteration methods [5] are the classical approach; however, these methods may have severe practical limitations due to the sensitivity to the initial guess and the required computational cost for large and strongly nonlinear systems [6, 7]. In the past years, the Selective Frequency Damping (SFD) method developed by Åkervik et al. [4] has arisen as a solid alternative. Its robustness and ease of implementation into existing time-stepping methods have made it increasingly popular to the point that it is generally the preferred method for aeronautical applications [8].

Based on control theory, SFD adds a linear forcing term to eq. (1), which drives the flow field $\boldsymbol{q}$ towards $\boldsymbol{q}_s$ [4]. As this target solution is not known beforehand, $\boldsymbol{q}_s$ is substituted by a low-pass filtered version of $\boldsymbol{q}$, denoted by $\bar{\boldsymbol{q}}$. The evolution equation for $\boldsymbol{q}$ is then rewritten as

$$\dot{\boldsymbol{q}} = f(\boldsymbol{q}) - \chi(\boldsymbol{q} - \bar{\boldsymbol{q}}), \qquad \chi \in \mathbb{R}^+. \tag{3}$$

The forcing is a linear reaction term proportional to the high-frequency content of the flow. Its effectiveness in quenching unstable frequencies and hence suppressing the associated instabilities depends on the feedback control coefficient χ. Åkervik et al. [4] suggest an exponential kernel filter to compute $\bar{\boldsymbol{q}}$. Since the implementation of the integral formulation of the filter would generally imply infeasible memory requirements in practice, its differential formulation is considered instead:

$$\dot{\bar{\boldsymbol{q}}} = \frac{\boldsymbol{q} - \bar{\boldsymbol{q}}}{\Delta}, \qquad \Delta \in \mathbb{R}^{+}. \tag{4}$$

The time constant Δ is related to the cut-off frequency (ω_c) of the low-pass filter through $\Delta = 1/\omega_c$. The performance of SFD depends on the two aforementioned parameters of the model, χ and Δ, which must be chosen as inputs of the simulation. Appropriate values depend on the flow problem and hence their selection is key to the method's effectiveness and efficiency as they determine the stability and convergence rate [4, 6, 9, 10]. Not every combination of χ and Δ guarantees that the flow field is driven towards the steady state, and even if so, the required computational time may be so large that the approach is impractical. Hence, how to select adequate χ and Δ is a common predicament in the literature.

SFD has nonetheless been very successfully applied to two- and three-dimensional flow configurations: Åkervik et al. [4] first applied the method for stabilising a separation bubble with success and the steady solution of a confined separated flow was obtained by Åkervik et al. [11]. Pier [12] computed the base flow around a sphere to analyse local and global instabilities developing in the wake. Schmid [13] analysed the stability of the flow in a square cavity by using a reference solution computed with SFD. Bagheri et al. [14] successfully applied SFD to stabilise a jet in crossflow and Fani et al. [15] found the base flow for a three-dimensional T-mixer. Loiseau et al. [16] studied roughness-induced transition by performing stability analyses using base-flow solutions computed with SFD. More recently, Richez et al. [8] applied SFD to stabilise RANS simulations of the turbulent separated flow around an airfoil at stall and Kurz and Kloker [17] computed with SFD the steady state of a three-dimensional boundary layer over a swept wing with roughness elements. Significant contributions to the advancement of the methodology where published by Jordi et al. [9], who developed an alternative SFD formulation, and Cunha et al. [6], who developed an optimisation method for SFD simulations based on Dynamic Mode Decomposition (DMD).

The model parameters χ and Δ are commonly based on rough estimations introduced by Åkervik et al. [4] or on parametric studies of simplified models. Jordi et al. [9, 10] used a scalar model problem to infer the behaviour of SFD when applied to a real flow problem. By using this model, Jordi et al. [9] generate stability curves identifying the influence of χ and Δ and indicate that SFD is incapable of stabilising steady unstable eigenmodes, corroborating the results of Vyazmina [18]. It was observed that increasing χ may not always guarantee convergence, contrary to the consensus introduced by Åkervik et al. [4]. Jordi et al. [10] hypothesised that the parameter values that optimise the scalar model problem also optimise the full flow problem and developed a coupled approach, which combines the computation of partially converged flow fields, stability analyses and parameter optimisation for the model problem. Cunha et al. [6] use DMD of the controlled flow field to determine parameters that minimise the growth rate of the least stable DMD mode.

There are cases in which SFD reportedly failed [18, 19]. It was claimed that cases in which the flow field presents steady unstable eigenmodes, SFD is unable to drive the simulation towards the steady state. Several authors indicate that too large χ yield infeasible simulation times [4, 6, 19]. Massa [20] and Teixeira and Alves [7] reported that stabilising a flow field that is unstable to more than one eigenmode can be a challenging task. In particular, Massa [20] claimed that SFD fails to converge towards the base flow if unstable eigenvalues with high amplification rates and low-frequency weakly unstable eigenvalues are both present in the flow field. In conclusion, a better understanding of χ and Δ is required to establish the feasibility of the method in the first place.

In this paper, the role played by χ and Δ is analysed in detail. We aim to answer the main open question presented by literature:

> Which values of χ and Δ are effective and most efficient?

Five follow-up questions immediately arise:

1. Does SFD fail to stabilise systems with unstable steady eigenmodes?
2. Does the method's feasibility depend on specific eigenvalue properties?
3. Given adequate Δ, does increasing χ always yield a stabilised system?
4. How can multiple discrete unsteady eigenmodes be accounted for?
5. What is the physical mechanism represented by the stabilised system?

The main findings presented in this article answer the aforementioned questions: in §3, we show that, in absence of steady unstable eigenmodes, SFD is always capable of stabilising globally unstable flow fields ruled by one (or

a complex conjugate pair of) unstable eigenmode(s). We derive formulas for χ and Δ that ensure convergence towards the steady state and thereby prove that SFD is unable to suppress steady instabilities. We show that the governing non-dimensional parameter is the ratio of the growth rate over the frequency of the unstable eigenvalue. This parameter rules the *difficulty* in stabilising the flow, which allows us to define a threshold for feasibility in practice. The analysis is then extended to flow configurations ruled by more than one unstable eigenmode. In §4 the flow unleash technique is described, which allows characterising the properties of the unstable eigenmode without performing an independent stability analysis. In §5, we introduce a parameter optimisation method based on the inference of the stability properties of the relevant eigenmodes. Analytical expressions are derived for χ and Δ that minimise the spectral radius of the simulation and scalar-problem-optimising parameters are demonstrated to be suboptimal. The method is generally applicable; here, it is tested for a two-dimensional incompressible cylinder flow. For this case a physical interpretation of the stabilisation mechanism is presented in §6.

2. Methodology

2.1. Original SFD formulation

Equations (3) and (4) can be discretised using any time-marching scheme. In case of convergence, $\boldsymbol{q}$ and $\bar{\boldsymbol{q}}$ have the same steady state, $\dot{\boldsymbol{q}}_s = \dot{\bar{\boldsymbol{q}}}_s = 0$ and $\boldsymbol{q}_s = \bar{\boldsymbol{q}}_s$. We therefore can use the difference between them as convergence criterion $\epsilon_{\mathrm{R}} = ||\boldsymbol{q} - \bar{\boldsymbol{q}}||_{L_2}$, with ϵ_{R} representing the so-called SFD residual of the simulation. As time progresses and $\epsilon_{\mathrm{R}} \to 0$, the linear forcing term in eq. (3) approaches zero and the steady solution of eq. (3) becomes identical to that of eq. (1). This guarantees that no artificial base flow solutions are created in spite of the fact that the system is changed. The (linear) dynamics of the modified system can be addressed through the linearisation of eqs. (3) and (4) yielding:

$$\begin{bmatrix} \dot{\boldsymbol{q}}' \\ \dot{\bar{\boldsymbol{q}}}' \end{bmatrix} = \underbrace{\begin{bmatrix} \boldsymbol{J} - \chi \boldsymbol{I} & \chi \boldsymbol{I} \\ \dfrac{\boldsymbol{I}}{\Delta} & -\dfrac{\boldsymbol{I}}{\Delta} \end{bmatrix}}_{\boldsymbol{G}} \begin{bmatrix} \boldsymbol{q}' \\ \bar{\boldsymbol{q}}' \end{bmatrix}, \tag{5}$$

where $\bar{\boldsymbol{q}}'$ indicates the perturbation of the $\bar{\boldsymbol{q}}$ field, $\boldsymbol{J}$ denotes the Jacobian of $f(\boldsymbol{q})$ around $\boldsymbol{q}_s$ and $\boldsymbol{I}$ denotes the identity operator. The relation between the eigenvalues $\mu = \mu_r + \mathrm{i}\mu_i$ of the original system, $-\mathrm{i}\boldsymbol{J}$, with the eigenvalues $\lambda = \lambda_r + \mathrm{i}\lambda_i$ of the modified system, $-\mathrm{i}\boldsymbol{G}$, was derived by Åkervik et al. [4] and is here rewritten as

$$\lambda_{1,2} = \frac{1}{2}\left(\mu - \mathrm{i}\chi - \frac{\mathrm{i}}{\Delta} \pm \frac{\mathrm{i}}{\Delta}\sqrt{\left(1 - \Delta[\mathrm{i}\mu + \chi]\right)^2 + 4\chi\Delta}\right), \qquad \mu, \lambda \in \mathbb{C}. \tag{6}$$

The subindices of $\lambda_{1,2}$ express that every original eigenvalue μ is mapped onto two λ eigenvalues. This is a consequence of doubling the dimension of the system by introducing $\bar{\boldsymbol{q}}$. Garnaud et al. [21] derived an expression for the inverse mapping, which maps the λ's back onto the μ's:

$$\mu = \lambda + \mathrm{i}\chi\left(1 - \frac{1}{1 - \mathrm{i}\lambda\Delta}\right). \tag{7}$$

The time independency of the linearised system permits prescribing the following ansatz for the perturbation field

$$\boldsymbol{q}'(\boldsymbol{x}, t) = \sum_{j=-\infty}^{\infty} A_j \underbrace{\tilde{\boldsymbol{q}}_j(\boldsymbol{x})\mathrm{e}^{-\mathrm{i}\mu^j t}}_{\boldsymbol{p}'_j(\boldsymbol{x},t)}, \quad A_j \in \mathbb{C}, \tag{8}$$

where A_j is the amplitude coefficient, and $\tilde{\boldsymbol{q}}_j(\boldsymbol{x})$ is the complex valued shape function corresponding to the j^{th} eigenvalue μ^j [2, 3] and $\mu^{-j} = -\overline{\mu^j}$. Accordingly, an eigenmode with associated eigenvalue μ is stable if $\mu_i < 0$, neutral if $\mu_i = 0$, and unstable if $\mu_i > 0$. The variable $\boldsymbol{p}'_j = \tilde{\boldsymbol{q}}_j(\boldsymbol{x})\mathrm{e}^{-\mathrm{i}\mu^j t}$ is introduced to include the temporal behaviour of the eigenmode.

The same exponential dichotomy applies to λ when considering the controlled SFD eigenspectrum. In that case $\tilde{\bar{\boldsymbol{q}}}$ represents the shape function corresponding to the eigenvalue λ. Åkervik et al. [4] observe that the controlled eigenvalues $\lambda_{1,2}$ have associated eigenvectors $\tilde{\bar{\boldsymbol{q}}}_{1,2}$ which are a phase-shifted version of $\tilde{\boldsymbol{q}}$. In fact $\tilde{\bar{\boldsymbol{q}}}_{1,2} = \beta_{1,2}\tilde{\boldsymbol{q}}$, where

$$\beta_{1,2} = 1 + \frac{\lambda_{1,2} - \mu}{\mathrm{i}\chi}. \tag{9}$$

This illustrates that the SFD eigenvalue problem does not introduce new eigenfunction shapes. The exponential temporal behaviour associated to $\tilde{\bar{\boldsymbol{q}}}_j$ will be expressed as $\bar{\boldsymbol{p}}'_j$.

2.2. Encapsulated formulation of SFD

The encapsulated formulation of SFD (hereafter referred to as ESFD) described by Jordi et al. [9] allows the application of SFD without modifying the core of Computational Fluid Dynamics (CFD) solvers. ESFD separates the linear and non-linear parts of eqs. (3) and (4):

$$\begin{bmatrix} \dot{\boldsymbol{q}} \\ \dot{\bar{\boldsymbol{q}}} \end{bmatrix} = \begin{bmatrix} f(\boldsymbol{q}) \\ \boldsymbol{0} \end{bmatrix} + \begin{bmatrix} -\chi\boldsymbol{I} & \chi\boldsymbol{I} \\ \dfrac{\boldsymbol{I}}{\Delta} & -\dfrac{\boldsymbol{I}}{\Delta} \end{bmatrix} \begin{bmatrix} \boldsymbol{q} \\ \bar{\boldsymbol{q}} \end{bmatrix} = \begin{bmatrix} f(\boldsymbol{q}) \\ \boldsymbol{0} \end{bmatrix} + \boldsymbol{T}\boldsymbol{D}\boldsymbol{T}^{-1} \begin{bmatrix} \boldsymbol{q} \\ \bar{\boldsymbol{q}} \end{bmatrix} \tag{10}$$

with

$$\boldsymbol{D} = \begin{bmatrix} \boldsymbol{0} & \boldsymbol{0} \\ \boldsymbol{0} & -\left(\chi + \dfrac{1}{\Delta}\right)\boldsymbol{I} \end{bmatrix} \qquad \text{and} \qquad \boldsymbol{T} = \begin{bmatrix} \boldsymbol{I} & -\chi\Delta\boldsymbol{I} \\ \boldsymbol{I} & \boldsymbol{I} \end{bmatrix}. \tag{11}$$

The non-linear subsystem contains the Navier-Stokes operator f, whose implementation in a CFD solver is represented by the functional Φ, that maps the discrete solution from a temporal state t^n to $t^{n+1} = t^n + \tau$. The linear subsystem is integrated analytically over the time step τ:

$$\begin{bmatrix} (\boldsymbol{q}^\star)^{n+1} \\ (\bar{\boldsymbol{q}}^\star)^{n+1} \end{bmatrix} = \begin{bmatrix} \Phi(\boldsymbol{q}^n) \\ \bar{\boldsymbol{q}}^n \end{bmatrix}; \quad \begin{bmatrix} \boldsymbol{q}^{n+1} \\ \bar{\boldsymbol{q}}^{n+1} \end{bmatrix} = \underbrace{\boldsymbol{T}\mathrm{e}^{\boldsymbol{D}\tau}\boldsymbol{T}^{-1}}_{\boldsymbol{H}} \begin{bmatrix} (\boldsymbol{q}^\star)^{n+1} \\ (\bar{\boldsymbol{q}}^\star)^{n+1} \end{bmatrix}, \tag{12}$$

where $\boldsymbol{q}^\star$ and $\bar{\boldsymbol{q}}^\star$ represent intermediate solutions of (3) and (4) when applying the splitting method and

$$\boldsymbol{H} = \frac{1}{1+\chi\Delta} \begin{bmatrix} \boldsymbol{I} + \chi\Delta\boldsymbol{I}\mathrm{e}^{-\left(\chi+\frac{1}{\Delta}\right)\tau} & \chi\Delta\boldsymbol{I}\left(1 - \mathrm{e}^{-\left(\chi+\frac{1}{\Delta}\right)\tau}\right) \\ \boldsymbol{I} - \boldsymbol{I}\mathrm{e}^{-\left(\chi+\frac{1}{\Delta}\right)\tau} & \chi\Delta\boldsymbol{I} + \boldsymbol{I}\mathrm{e}^{-\left(\chi+\frac{1}{\Delta}\right)\tau} \end{bmatrix} = \begin{bmatrix} h_{11}\boldsymbol{I} & h_{21}\boldsymbol{I} \\ h_{12}\boldsymbol{I} & h_{22}\boldsymbol{I} \end{bmatrix}. \tag{13}$$

2.3. Parametrisation of the behaviour of SFD

Equation (6) links the linearised dynamics of the original system and that of the controlled system. For a complete characterisation of the functionality of SFD, it is necessary to establish another link between the exact linearised system dynamics and the discrete numerical solutions. First and foremost, a main objective is to find χ and Δ that stabilise the numerically represented system. However, the inverse approach is also of interest. When a simulation performed using SFD does not converge towards the base flow, it may be because the flow's inherent unsteady nature is not completely quenched (physical instability), due to the numerical methods used to integrate the controlled system (numerical instability), or a combination of both.

Cunha et al. [6] state that, under certain conditions, the spectral properties of eq. (5) can be represented as superposition of mono-modal problems, for which eq. (5) is assumed equivalent to

$$\begin{bmatrix} \dot{\boldsymbol{p}'}_j \\ \dot{\bar{\boldsymbol{p}}'}_j \end{bmatrix} = \underbrace{\begin{bmatrix} (-\mathrm{i}\mu^j - \chi)\boldsymbol{I} & \chi\boldsymbol{I} \\ \dfrac{\boldsymbol{I}}{\Delta} & -\dfrac{\boldsymbol{I}}{\Delta} \end{bmatrix}}_{\boldsymbol{G}_j} \begin{bmatrix} \boldsymbol{p}'_j \\ \bar{\boldsymbol{p}}'_j \end{bmatrix}, \qquad j = 1, 2, \ldots, \infty. \tag{14}$$

Two main approaches are presented next to characterise the eigenvalues α associated to an SFD simulation. By integrating eq. (14) between two temporal states t^n and t^{n+1}, one obtains

$$\begin{bmatrix} (\boldsymbol{p}'_j)^{n+1} \\ (\bar{\boldsymbol{p}}'_j)^{n+1} \end{bmatrix} = \mathrm{e}^{\boldsymbol{G}_j\tau} \begin{bmatrix} (\boldsymbol{p}'_j)^{n} \\ (\bar{\boldsymbol{p}}'_j)^{n} \end{bmatrix} = \boldsymbol{B}_j \begin{bmatrix} (\boldsymbol{p}'_j)^{n} \\ (\bar{\boldsymbol{p}}'_j)^{n} \end{bmatrix}, \qquad j = 1, 2, \ldots, m. \tag{15}$$

The exact eigenvalues of $\boldsymbol{B}_j = \mathrm{e}^{\boldsymbol{G}_j\tau}$ are

$$\alpha^j_{\mathrm{ex}_{1,2}} = \mathrm{e}^{-\mathrm{i}\lambda^j_{1,2}\tau}. \tag{16}$$

We see that only pairs of χ and Δ values which locate all $\lambda_{1,2}$ in the lower half-plane lead to convergence.

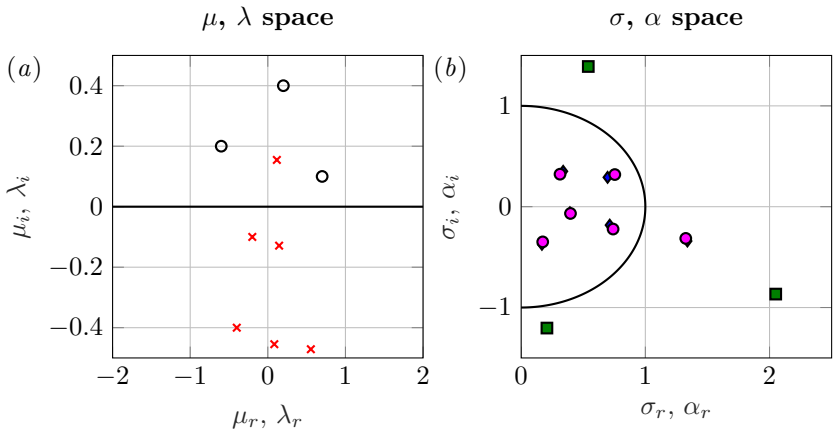

Figure 1: Eigenvalue spaces relevant in SFD: μ (empty circles), λ (red crosses), σ (green squares), α_{ex} (purple circles) and α_{num} (blue diamonds). $\mu^j = 0.2 + 0.4\text{i};\ -0.6 + 0.2\text{i};\ 0.7 + 0.1\text{i}$, $\sigma^j = \text{e}^{-\text{i}\mu^j\tau}$, $\chi = 0.5$, $\Delta = 5$ and $\tau = 2$.

The ESFD formulation applied to eq. (14) can be written as:

$$\begin{bmatrix} (\boldsymbol{p}'_j)^{n+1} \\ (\bar{\boldsymbol{p}}'_j)^{n+1} \end{bmatrix} = \underbrace{\begin{bmatrix} h_{11}\boldsymbol{I} & h_{21}\boldsymbol{I} \\ h_{12}\boldsymbol{I} & h_{22}\boldsymbol{I} \end{bmatrix} \begin{bmatrix} \sigma^j\boldsymbol{I} & \boldsymbol{0} \\ \boldsymbol{0} & \boldsymbol{I} \end{bmatrix}}_{\boldsymbol{C}_j} \begin{bmatrix} (\boldsymbol{p}'_j)^{n} \\ (\bar{\boldsymbol{p}}'_j)^{n} \end{bmatrix} \quad j = 1, 2, \ldots, m. \tag{17}$$

Accordingly, $\sigma^j \in \mathbb{C}$ takes the role of Φ and represents the operator that numerically integrates the subsystem defined by $\dot{\boldsymbol{p}}'_j = -\text{i}\mu^j \boldsymbol{p}'_j$, such that $(\boldsymbol{p}'^{\star}_j)^{n+1} = \sigma^j (\boldsymbol{p}'_j)^n$ in the intermediate step of ESFD. Examples of possible expressions for σ^j are:

$$\sigma^j = \text{e}^{-\text{i}\mu^j\tau} \qquad \text{(exact solver)},$$

$$\sigma^j = 1 - \text{i}\mu^j\tau \qquad \text{(explicit Euler)},$$

$$\sigma^j = 1 - \text{i}\mu^j\tau - \tfrac{1}{2}(\mu^j\tau)^2 + \tfrac{1}{6}\text{i}(\mu^j\tau)^3 \quad \text{(3rd-order explicit Runge-Kutta)}.$$

The coefficients h_{11}, h_{12}, h_{21} and h_{22} are linked to the action of the filter and the proportional controller in eqs. (3) and (4) and σ^j condenses the information of the numerical time marching scheme. Therefore, the combined physical and numerical stability is characterised through the eigenvalues of $\boldsymbol{C}_j$, which read

$$\alpha^j_{\text{num}_{1,2}} = \frac{1}{2}\left(h_{11}\sigma^j + h_{22} \pm \sqrt{(h_{11}\sigma^j - h_{22})^2 + 4h_{12}h_{21}\sigma^j}\right). \tag{18}$$

The numerical solution of (3) and (4) can only converge towards the steady state if all $\alpha^j_{\text{num}_{1,2}}$ satisfy $|\alpha^j_{\text{num}_{1,2}}| < 1$.

The different eigenvalue spaces are summarised in figure 1. The original formulation of SFD, in which the coupled problem is solved without discretisation and splitting error, is represented by a $\mu \mapsto \lambda \mapsto \alpha_{\text{ex}}$ mapping. ESFD corresponds to a $\mu \mapsto \sigma \mapsto \alpha_{\text{num}}$ mapping. Even with an exact time marching method, $\sigma^j = \text{e}^{-\text{i}\mu^j\tau}$, $\alpha_{\text{num}} \neq \alpha_{\text{ex}}$ due to the fact that

$$\begin{bmatrix} -\text{i}\mu^j & 0 \\ 0 & 0 \end{bmatrix} \text{ and } \begin{bmatrix} -\chi & \chi \\ 1/\Delta & -1/\Delta \end{bmatrix}$$

do not commute and thus $\boldsymbol{B}_j \neq \boldsymbol{C}_j$, see [22]. However, $\alpha_{\text{num}} \to \alpha_{\text{ex}}$ as $\tau \to 0$ and accordingly α_{ex} is considered representative for α_{num} if conditionally stable time marching methods are used.

The characterisation of the eigenvalues α and the structure of the discretised system presented above allows to parametrise the evolution of the residual of an SFD simulation. After an initial transient, $\epsilon_R(t)$ follows an exponential trend proportional to the growth rate of the least stable eigenvalue of the controlled eigenspectrum, which we denote by λ^{s}.

3. Analysis

3.1. Effective stabilisation of isolated unstable eigenmodes

In the present section, the influence of χ and Δ is analysed by studying the $\mu \mapsto \lambda$ mapping. For the sake of simplicity, we first assume that only one instability mode is present in the flow field. The stabilisation of flow configurations with more than one unstable eigenmode is tackled in subsection 3.2.

The eigenvalues of the controlled system, $\lambda_{1,2}$, are the solutions of the quadratic equation

$$\lambda^2 + \left(\mathrm{i}\left(\chi + \frac{1}{\Delta}\right) - \mu\right)\lambda - \frac{1}{\Delta}\mathrm{i}\mu = 0, \tag{19}$$

from which the two useful expressions

$$\lambda_1 + \lambda_2 = \mu - \mathrm{i}\left(\chi + \frac{1}{\Delta}\right) \quad \text{and} \quad \lambda_1\lambda_2 = -\frac{1}{\Delta}\mathrm{i}\mu \tag{20}$$

can be immediately derived by using Vieta's formulas.

Åkervik et al. [4] indicate that χ should be larger than the growth rate of the unstable modes present in the flow field and that $1/\Delta$ ought to be smaller than the frequency of these modes. We denote the most unstable eigenvalue associated to a flow configuration with μ^{c}. As $\mu_i^{\mathrm{c}} > 0$, the parameters are expected to scale with μ^{c}, in such a way that $\chi \sim \mu_i^{\mathrm{c}}$ and $1/\Delta \sim \mu_r^{\mathrm{c}}$. Accordingly, eqs. (20) can be rewritten in non-dimensional form considering the following change of variables:

$$\hat{\chi} = \frac{\chi}{\mu_i^{\mathrm{c}}}, \qquad \hat{\Delta} = \Delta\mu_r^{\mathrm{c}}, \qquad \hat{\lambda}_r = \frac{\lambda_r}{\mu_r^{\mathrm{c}}}, \qquad \hat{\lambda}_i = \frac{\lambda_i}{\mu_i^{\mathrm{c}}}, \tag{21}$$

such that

$$\hat{\lambda}_{1,r} + \hat{\lambda}_{2,r} = 1, \quad \hat{\lambda}_{1,r}\hat{\lambda}_{2,r} - \left(\frac{\mu_i^{\mathrm{c}}}{\mu_r^{\mathrm{c}}}\right)^2 \hat{\lambda}_{1,i}\hat{\lambda}_{2,i} = \frac{\mu_i^{\mathrm{c}}}{\mu_r^{\mathrm{c}}}\frac{1}{\hat{\Delta}}, \tag{22}$$

$$\hat{\lambda}_{1,i} + \hat{\lambda}_{2,i} = 1 - \hat{\chi} - \left(\frac{\mu_i^{\mathrm{c}}}{\mu_r^{\mathrm{c}}}\right)^{-1}\frac{1}{\hat{\Delta}}, \quad \hat{\lambda}_{1,i}\hat{\lambda}_{2,r} + \hat{\lambda}_{1,r}\hat{\lambda}_{2,i} = -\left(\frac{\mu_i^{\mathrm{c}}}{\mu_r^{\mathrm{c}}}\right)^{-1}\frac{1}{\hat{\Delta}}. \tag{23}$$

It becomes obvious that the non-dimensional expressions that define the $\mu \mapsto \lambda$ mapping depend only on the single non-dimensional parameter $(\mu_i^{\mathrm{c}}/\mu_r^{\mathrm{c}})$; the equations are self-similar when $\mu_i^{\mathrm{c}}/\mu_r^{\mathrm{c}}$ is kept constant.

By operating on eqs. (6) and (20), the following asymptotic behaviour can be derived:

$$\left.\begin{array}{l} \lim\limits_{\chi\to 0}\lambda_{\mathrm{n}} = \mu \\ \lim\limits_{\chi\to 0}\lambda_{\mathrm{a}} = -\dfrac{\mathrm{i}}{\Delta} \end{array}\right\} \qquad \left\{\begin{array}{l} \lim\limits_{\chi\to\infty}\lambda_1 = 0 \\ \lim\limits_{\chi\to\infty}\lambda_2 = \mu_r - \mathrm{i}\infty \end{array}\right. \tag{24}$$

which reveal the structure of the two λ branches resulting from the complex square root in eq. (6). In the limit when $\chi \to 0$ (linear forcing vanishes), one class of λ solutions corresponds to each of the natural μ eigenvalues, hence denoted by λ_{n}. The complementary λ_{a} eigenvalues are artificial solutions associated to the filter and degenerate to a point located at $-\mathrm{i}/\Delta$ if $\chi \to 0$. When $\chi \to \infty$, one set of λ solutions tends to minus infinity in their imaginary part and μ_r in their real part, while there is another group that moves towards the origin. The notation λ_1 and λ_2 in eq. (24) shall indicate that it is generally not possible to continuously track the natural branch (i.e., the one associated to μ when $\chi \to 0$) or the artificial branch (i.e., the one associated to $-\mathrm{i}/\Delta$ when $\chi \to 0$) when $\chi \to \infty$. This is illustrated in figure 2(b). A major part of the analysis presented in this article relies on this asymptotic behaviour. The complementary limiting behaviour in terms of Δ is

$$\left.\begin{array}{l} \lim\limits_{\Delta\to\infty}\lambda_1 = 0 \\ \lim\limits_{\Delta\to\infty}\lambda_2 = \mu - \mathrm{i}\chi \end{array}\right\} \qquad \left\{\begin{array}{l} \lim\limits_{\Delta\to 0}\lambda_{\mathrm{n}} = \mu \\ \lim\limits_{\Delta\to 0}\lambda_{\mathrm{a}} = 0 - \mathrm{i}\infty \end{array}\right. \tag{25}$$

The present approach is limited to flow fields ruled by instabilities with $\mu_r \neq 0$, which is conform with the low-pass filter nature of the stabilisation term. Many authors conclude that SFD is unable to stabilise steady

eigenmodes, [6, 9, 18]. This is confirmed by analysing the $\mu \mapsto \lambda$ mapping, when imposing $\mu = \mathrm{i}\mu_i$. For this particular case, the $\lambda_{1,2}$ solutions are always purely imaginary and never intersect with each other. Recalling eq. (20), $\lambda_{1,i}\lambda_{2,i} = -\mu_i/\Delta$ and if $\mu_i > 0$, regardless of χ and Δ, it is impossible to place both $\lambda_{1,2}$ solutions within the stable region.

Another fundamental property of SFD is that a stable μ will never be mapped towards the upper semi-plane. By manipulating the expression of the inverse mapping, eq. (7), a criterion can be derived relating the real parts of μ and the associated $\lambda_{1,2}$ solutions:

$$\frac{\mu_r}{\lambda_r} = 1 + \frac{\chi\Delta}{\left(1+\lambda_i\Delta\right)^2 + \left(\lambda_r\Delta\right)^2} \geq 1, \tag{26}$$

which proves that μ_r, $\lambda_{1,r}$ and $\lambda_{2,r}$ share signs and that $|\lambda_r| \leq |\mu_r|$. By using this result and imposing $\mu_i < 0$, the real part of eq. (20) requires that $\lambda_{1,i}\lambda_{2,i} > 0$. The imaginary part of eq. (20) conclusively requires $\lambda_{1,i} < 0$ and $\lambda_{2,i} < 0$, proving the statement of Åkervik et al. [4], that stable μ eigenvalues cannot yield unstable $\lambda_{1,2}$ solutions.

Next, it is analysed how each $\lambda_{1,2}$ solution evolves by fixing Δ at different discrete positive values, taking χ as a real continuous variable with $\chi \in [0, \infty)$ and assuming $\mu_r^{\mathrm{c}} \neq 0$, see figure 2($a$). Figure 2($b$) contains four pairs of branches representative of the whole λ solution space. Figure 2(c) complements the results with the gradients with respect to χ of the $\lambda_{1,2}$ solution branches, i.e.,

$$\frac{\partial\lambda_{1,2}}{\partial\chi} = \frac{1}{2}\mathrm{i}\left(-1 \pm \frac{\Delta(\mathrm{i}\mu+\chi)+1}{\sqrt{\left(1-\Delta[\mathrm{i}\mu+\chi]\right)^2 + 4\chi\Delta}}\right). \tag{27}$$

For every μ with $\mu_r \neq 0$, there exists a unique pair of real and positive χ and Δ values for which $\lambda_1 = \lambda_2$. These special SFD parameters are hereafter denoted by $\chi^\star$ and $\Delta^\star$. The key ingredient to find adequate SFD parameters is that the critical point

$$\lambda^\star = \frac{1}{2}\mu_r^{\mathrm{c}} - \frac{\mathrm{i}}{\Delta^\star}. \tag{28}$$

is always located within the stable region, regardless of μ^{c}. When applying

$$\chi^\star = \frac{|\mu^{\mathrm{c}}| + \mu_i^{\mathrm{c}}}{2}, \tag{29}$$

$$\Delta^\star = \frac{2}{|\mu^{\mathrm{c}}| - \mu_i^{\mathrm{c}}} \tag{30}$$

as parameters of the model, the associated $\lambda_{1,2}$ solutions are both mapped towards $\lambda^\star$ and hence they are always located in the real direction at half of the real part of μ^{c} and at an imaginary coordinate coinciding with the origin of the artificial branch, see figure 2(b). Due to the fact that $\lambda^\star$ is located in the lower half-plane for any unstable μ^{c}, the parameter choice $\chi = \chi^\star$ and $\Delta = \Delta^\star$ will always stabilise the linear flow problem in an exponential sense, asymptotically in time.

The case $\Delta = \Delta^\star$, represented by the solid black line in figure 2, establishes a threshold separating two main trends of the solution branches. Considering $\Delta < \Delta^\star$, the natural branch approaches the origin as χ grows, whereas the artificial branch tends to $-\mathrm{i}\infty$. The dash-dotted line and the dotted line in figure 2 correspond to subcritical cases following the aforementioned trend. The dash-dotted natural branch never crosses the real axis; the associated eigenvalues never become stable. On the other hand, there is a specific χ-range for which the dotted branch of natural λ solutions are located within the stable region. For sufficiently large χ values, the dotted natural branch solution crosses the real axis a second time. The real axis is not crossed for larger χ, so increasing the control coefficient further will be counter productive. For $\Delta > \Delta^\star$, the overall trend is inverse; the artificial branch approaches 0 from the upper semi-plane when $\chi \to \infty$, whereas the natural branch tends to $-\mathrm{i}\infty$. The dashed line in figure 2 is representative of this supercritical behaviour. Besides the structure of the branches, another relevant difference exists between subcritical and supercritical cases. For $\Delta < \Delta^\star$ the dominant eigenvalue is always associated with the natural branch, thus changing continuously with χ. Contrarily, for $\Delta > \Delta^\star$ this role switches from one branch to the other; as χ is increased, the artificial branch claims dominance over the natural branch as the imaginary parts of the eigenvalues intersect.

Åkervik et al. [4] claim that very large χ will always drive the system towards the base solution, but possibly at a low convergence rate. The present results prove that this is not the case. Regardless of whether the case is

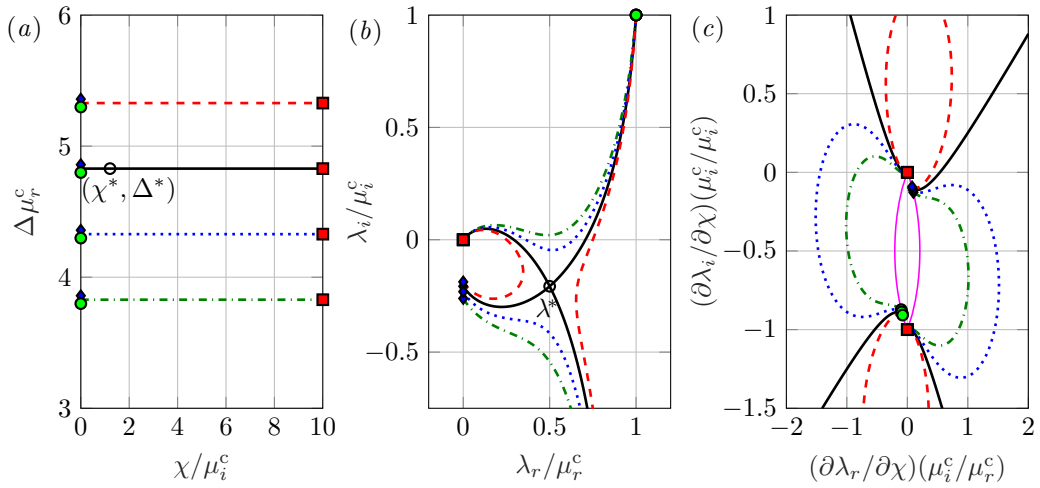

Figure 2: (a) χ and Δ, (b) solution branches in the λ space and (c) solution branches in the $\partial\lambda/\partial\chi$ space. Start of the natural branches (green circles), start of the artificial branches (blue diamonds), end points of all solutions (red squares), coordinates of $\chi^\star$ and $\Delta^\star$ in (a) and $\lambda^\star$ in (b) (empty circles). $\Delta\mu^c = 3.83$ (dash-dotted green), 4.33 (dotted blue), 4.83 (solid black), 5.33 (dashed red). Curve encompassing all start and end points of the $\partial\lambda_{1,2}/\partial\chi$ branches in (c) (magenta).

subcritical or supercritical, there is always a branch that for large χ approaches the origin from above, yielding unstable eigenvalues. In figure 2(c), the branches of the gradient field approaching 0 for growing χ cross the real axis close to the origin, and thereafter always yield $\partial\lambda_i/\partial\chi < 0$. This may, at a first glance, seem surprising as we just proved that no stable μ can be mapped onto the unstable region; however, a λ solution associated to an *unstable* μ eigenvalue may switch from one region to another depending on the selected values of χ and Δ.

These results, which are graphically observed in figure 2, can also be proven by considering the complex argument of $\lambda_1\lambda_2 = -\frac{1}{\Delta}\mathrm{i}\mu$, cf. eq. (20),

$$\varphi_1 + \varphi_2 = \arg\left(-\frac{1}{\Delta}\mathrm{i}\mu\right) = -\arctan\left(\frac{\mu_r}{\mu_i}\right) = \arctan\left(\frac{\mu_i}{\mu_r}\right) - \frac{\pi}{2} = \varphi_\mu - \frac{\pi}{2} \tag{31}$$

with φ_1 and φ_2 denoting the arguments of λ_1 and λ_2 respectively; φ_μ represents the argument associated to the eigenvalue μ. Equation (31) shows that for a given μ, the sum of the arguments of the $\lambda_{1,2}$ solutions is constant and independent of χ and Δ. In particular, (31) implies that the constant value must correspond to $\varphi_1+\varphi_2$, and can be conveniently evaluated for $\chi \to 0$, where the angle associated to the natural solution is φ_μ and the angle associated to the artificial solution is $\arg(-\mathrm{i}/\Delta) = -\pi/2$. Evaluating the $\lambda_{1,2}$ solutions for $\chi \to \infty$, eq. (31) becomes

$$\lim_{\chi\to\infty}\varphi_1 + \lim_{\chi\to\infty}\varphi_2 = \lim_{\chi\to\infty}\varphi_1 + \underbrace{\lim_{\lambda_{2,i}\to-\infty}\left(\arctan\left(\frac{\lambda_{2,i}}{\mu_r}\right)\right)}_{-\pi/2} = \varphi_\mu - \frac{\pi}{2}, \tag{32}$$

assuming, without loss of generality, that $\mu_r^c > 0$. This conclusively implies:

$$\lim_{\chi\to\infty}\varphi_1 = \varphi_\mu = \arctan\left(\frac{\mu_i}{\mu_r}\right). \tag{33}$$

That is, the solution branch that approaches the origin follows an asymptote having the same argument as μ. If $\mu_i > 0$, $\varphi_\mu > 0$ and the least stable branch always approaches 0 from the upper semi-plane. Thus, choosing large χ yields unstable behaviour of the system.

3.2. Stabilisation of systems with more than one unstable eigenmode

The parameters $\chi^\star$ and $\Delta^\star$ always stabilise a flow field ruled by one unstable eigenvalue μ^c, under the condition $\mu_r^c \neq 0$. The present section extends the analysis to cases ruled by more than one unstable eigenmode. It is initially assumed that N unstable μ eigenvalues associated to the uncontrolled system are located in the upper half-plane. The most unstable eigenvalue, i.e., the one with the highest growth rate μ_i, is denoted by μ^c, while the other

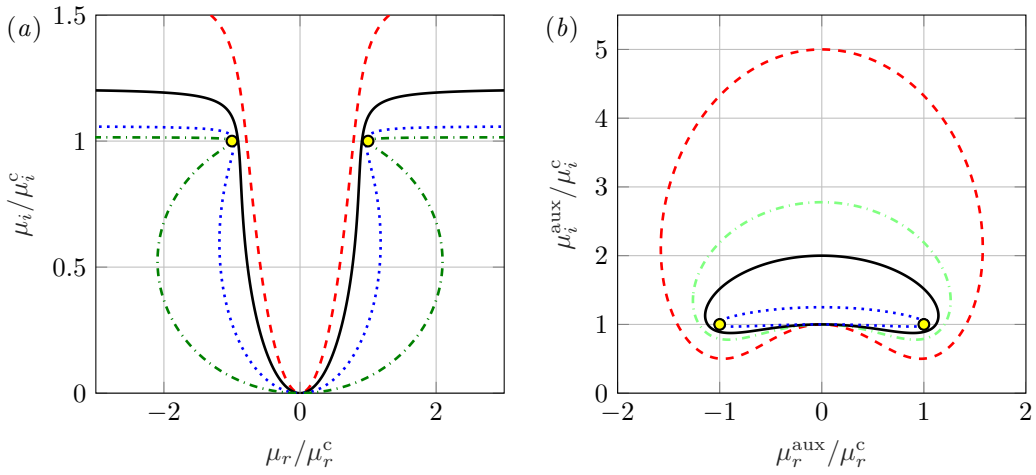

Figure 3: Stability curves in the μ space using (35). (a) μ eigenvalues mapped towards neutral λ_1 or λ_2 with $\chi = \chi^\star(\mu^c)$ and $\Delta = \Delta^\star(\mu^c)$. (b) regions encompassing μ^{aux} for which $\chi = \chi^\star(\mu^{aux})$ and $\Delta = \Delta^\star(\mu^{aux})$ will stabilise μ^c. μ_i^c/μ_r^c: 0.5 (dashed red); 0.75 (dash-dotted light green); 1 (solid black); 2 (dotted blue) and 4 (dashed-dotted dark green). μ^c (yellow circles).

unstable eigenvalues are denoted by μ^k, $k \in \{1, 2, \ldots, N-1\}$, and satisfy $\mu_i^c \geq \mu_i^k > 0$. The proposed methodology relies on applying $\chi^\star$ and $\Delta^\star$ as parameters of the model using μ^c in eqs. (29) and (30), due to the fact that μ^c is by definition the most critical eigenvalue to be stabilised. Thereafter, the part of the μ space that is mapped into the stable region is analytically determined.

For that purpose, eq. (20) is used in combination with two restrictive conditions: the model parameters are determined as $\chi = \chi^\star(\mu^c)$ and $\Delta = \Delta^\star(\mu^c)$ and the bounding curve of the stability domain (loci of neutral stability) is determined by imposing that either $\lambda_{1,i} = 0$ or $\lambda_{2,i} = 0$. The results are independent of the latter choice due to the symmetry of the problem. Two intermediate results can be immediately derived:

1. For a generic unstable μ, when one of its associated λ solutions lies on the real axis, the complementary λ solution is stable. This validates the usage of the condition $\lambda_{1,i} = 0$ or $\lambda_{2,i} = 0$ to define stability regions in the μ space.
2. The complementary λ solution satisfies
$$\lambda_r \mu_r = -\lambda_i \mu_i, \tag{34}$$
meaning that the lines connecting the origin of the complex plane with a generic unstable μ and its associated stable λ are orthogonal.

The geometrical curve encompassing the μ eigenvalues for which one λ solution is neutral satisfies

$$\left(\frac{\mu_i}{\mu_r}\right)^3 - 2\left(\frac{\mu_i}{\mu_r}\right)^2 \frac{|\mu^c|}{\mu_r} + \left(\frac{\mu_i}{\mu_r}\right)\left(1 + \frac{|\mu^c|^2}{\mu_r^2}\right) - \frac{1}{2\mu_r}\left(|\mu^c| + \mu_i^c\right) = 0. \tag{35}$$

Figure 3(a) shows four examples of curves plotted following eq. (35). As stated earlier, the SFD mapping is self-similar with respect to the parameter μ_i^c/μ_r^c. Thus the curves maintain their shape for constant μ_i^c/μ_r^c. All μ^k below the curves will be stabilised, while those located above will remain unstable in the λ space.

The cases in which one or more μ^k have large μ_i^k/μ_r^k (relative to μ_i^c/μ_r^c), are potential candidates to remain unstable, as can be inferred from figure 3(a). A possible solution to this is to define an auxiliary value, $\mu^{aux} \in \mathbb{C}$, which may not correspond to any physical eigenmode of the flow, but $\chi^\star(\mu^{aux})$ and $\Delta^\star(\mu^{aux})$ could lead to a global stabilisation. For that purpose, equation (35) can be used inversely. Another approach is to determine the values $\mu^{aux} = \mu_r^{aux} + i\mu_i^{aux}$ for which the corresponding $\chi^\star$ and $\Delta^\star$ imply neutral $\lambda_{1,i}(\mu^c)$ or $\lambda_{2,i}(\mu^c)$. Figure 3(b) plots limiting curves computed following this second approach.

When aiming to stabilise μ^c and all μ^k, the intersection of all regions encompassed by the μ^{aux} boundaries has to be found, if it is not empty. Figure 4 shows that the parameter choice $\chi = \chi^\star(\mu^c)$ and $\Delta = \Delta^\star(\mu^c)$ or $\chi = \chi^\star(\mu^k)$ and $\Delta = \Delta^\star(\mu^k)$ cannot lead to a global stabilisation of the system. However, for the case in figure 4(a) there exists a complementary finite range of χ and Δ for which SFD stabilises the system.

Particularly relevant are the μ^{aux} when curves of figure 3(b) cross the imaginary axis. Denoting l_u and l_l as the upper and lower limits respectively, and operating on eq. (35) using the second approach described above, it is

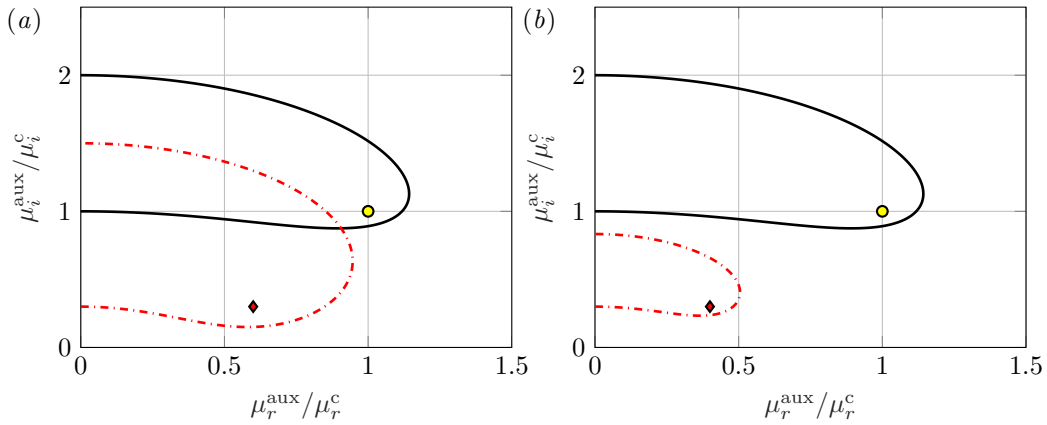

Figure 4: Limiting curves defining the sets of μ^{aux} values stabilising μ^{c} or μ^{k} if $\chi = \chi^\star(\mu^{\mathrm{aux}})$ and $\Delta = \Delta^\star(\mu^{\mathrm{aux}})$ are chosen. $\mu^{\mathrm{c}} = 1+1\mathrm{i}$ (yellow circles, solid black), $\mu^{\mathrm{k}} = 0.6 + 0.3\mathrm{i}$ (a), $\mu^{\mathrm{k}} = 0.4 + 0.3\mathrm{i}$ (b) (red diamonds, dash-dotted red).

possible to show that

$$l_{\mathrm{u}}(\mu^{\mathrm{c}}) = \frac{|\mu^{\mathrm{c}}|^2}{\mu_i^{\mathrm{c}}}, \quad l_{\mathrm{l}}(\mu^{\mathrm{c}}) = \mu_i^{\mathrm{c}}, \tag{36}$$

such that the non-dimensional distance between l_{u} and l_{l} is:

$$\frac{l_{\mathrm{u}}(\mu^{\mathrm{c}}) - l_{\mathrm{l}}(\mu^{\mathrm{c}})}{\mu_i^{\mathrm{c}}} = \left(\frac{\mu_i^{\mathrm{c}}}{\mu_r^{\mathrm{c}}}\right)^{-2}. \tag{37}$$

This result highlights the relevance of the non-dimensional parameter $\mu_i^{\mathrm{c}}/\mu_r^{\mathrm{c}}$ once again. As shown in figure 3(b), the length defined by $l_{\mathrm{u}}(\mu^{\mathrm{c}}) - l_{\mathrm{l}}(\mu^{\mathrm{c}})$ can be considered indicative of the broadness of the range of χ and Δ values that drive the system towards the base flow. If μ^{c} is unknown initially and χ and Δ ought to be tested by trial-and-error, the stabilisation of flow fields ruled by a μ^{c} with a large complex argument will be difficult. Furthermore, from the topology of the limiting curves in figure 3(b), it follows that SFD will only stabilise a flow field ruled by more than one unstable eigenmode if

$$l_{\mathrm{l}}(\mu^{\mathrm{c}}) \leq l_{\mathrm{u}}(\mu^{\mathrm{k}}), \tag{38}$$

which implies

$$\mu_i^{\mathrm{c}} \leq \frac{|\mu^{\mathrm{k}}|^2}{\mu_i^{\mathrm{k}}} = \frac{|\mu^{\mathrm{k}}|}{\sin\varphi_{\mathrm{k}}} = |\mu^{\mathrm{k}}|\sqrt{1 + \left(\frac{\mu_i^{\mathrm{k}}}{\mu_r^{\mathrm{k}}}\right)^{-2}}, \tag{39}$$

with φ_{k} being the argument of a given μ^{k}. This result confirms the trend observed in figure 3(a). For SFD to be able to drive the system towards the base flow when several unstable eigenvalues are present, all μ^{k} are required to have a small $\mu_i^{\mathrm{k}}/\mu_r^{\mathrm{k}}$ ratio and a large modulus relative to μ_i^{c}. Equation (39) indicates under which conditions the statement given by Massa [20], claiming that SFD fails to stabilise flow fields ruled by large growth rates and low-frequency low-energy eigenmodes, holds. We see that the difficulty does not strictly come from a growth rate difference, but from the presence of μ^{k} with large $\mu_i^{\mathrm{k}}/\mu_r^{\mathrm{k}}$ value located close to the origin.

3.3. Feasibility and required accuracy

Refocussing the attention on flow problems ruled by one unstable μ^{c} with $\mu_r^{\mathrm{c}} \neq 0$, the parameters $\chi^\star$ and $\Delta^\star$ always effectively stabilise the problem. In practice, however, the effectiveness depends on the accuracy of the available estimate for μ^{c}. Accordingly, the sensitivity of $\chi^\star$ and $\Delta^\star$ with respect to the input parameter μ^{c} for a flow problem unstable to a single discrete eigenmode is of high relevance. We consider the perturbed eigenvalue:

$$\mu^\epsilon = \mu(1+\epsilon) = \mu_r(1+\epsilon) + \mathrm{i}\mu_i(1+\epsilon), \quad |\epsilon| \ll 1. \tag{40}$$

Evaluating $\chi_\epsilon^\star = \chi^\star(\mu^\epsilon)$ and $\Delta_\epsilon^\star = \Delta^\star(\mu^\epsilon)$ for different values of the error parameter ϵ, the regions of the μ eigenspectrum having one of their associated λ solutions on the real axis (neutral stability) are determined. This

Eigenvalue argument	Affordable error	Stabilisation difficulty
$\mu_i^c/\mu_r^c < 1.12$	$\epsilon_{\max} > 10\%$	easy
$2.82 > \mu_i^c/\mu_r^c > 1.12$	$10\% > \epsilon_{\max} > 1\%$	
$\mu_i^c/\mu_r^c > 2.82$	$\epsilon_{\max} < 1\%$	hard

Table 1: Classification of flow instabilities based on the required accuracy in the computation of $\chi^\star$ and $\Delta^\star$ to guarantee convergence towards the steady state.

approach resembles that presented in §3.2. By operating on eq. (20), applying $\chi = \chi_\epsilon^\star$ and $\Delta = \Delta_\epsilon^\star$ and setting $\lambda_{1,i} = 0$ or $\lambda_{2,i} = 0$, the following condition is derived:

$$(1+\epsilon_{\max})^2 - \frac{\frac{\mu_i}{\mu_r} + \left(1+4\left(\frac{\mu_i}{\mu_r}\right)^2\right)\sqrt{1+\left(\frac{\mu_i}{\mu_r}\right)^2}}{2\frac{\mu_i}{\mu_r}\left(1+4\left(\frac{\mu_i}{\mu_r}\right)^2\right)}(1+\epsilon_{\max}) + 1 = 0. \tag{41}$$

The solutions of the quadratic equation (41) indicate the maximum allowed relative error $\epsilon_{\max}$ for a given eigenvalue μ that is aimed to be stabilised. Fundamental for the present analysis is the fact that eq. (41) only depends on the non-dimensional parameter μ_i/μ_r. Accordingly, all μ eigenvalues with an equal argument have a common tolerance and, as a consequence, share the same difficulty to be stabilised when using SFD. The higher μ_i/μ_r, the smaller $\epsilon_{\max}$ and the higher the required relative digital precision of μ^c, $\chi^\star$ and $1/\Delta^\star$. Small relative perturbations around the required true values of $\chi^\star$ and $\Delta^\star$ may lead to ineffectiveness for cases ruled by an instability with a large μ_i^c/μ_r^c. These results are linked to the behaviour of the limiting curves shown in figure 3(b); the higher μ_i^c/μ_r^c, the closer the curves to μ^c. A classification of instabilities based on the feasibility of SFD is presented in table 1.

4. The flow unleash technique

4.1. Methodology

Accurately determining the parameter μ^c requires a stability analysis, in turn requiring the base flow. We present a new technique, here referred to as *flow unleash*, through which we can accurately estimate μ^c with only one SFD or ESFD simulation. The unleash technique relies on driving the controlled simulation to a low enough residual level $\epsilon_R = ||\boldsymbol{q} - \bar{\boldsymbol{q}}||_{L_2}$ at time $t = t_u$. Then we continue the simulation for $t \geq t_u$ with $\chi = 0$ and maintain $\bar{\boldsymbol{q}}$ constant and equal to the last converged value, i.e., $\bar{\boldsymbol{q}}(\boldsymbol{x}, t) = \bar{\boldsymbol{q}}(\boldsymbol{x}, t_u)$ for $t \geq t_u$. By setting the control coefficient to $\chi = 0$, residual disturbances can grow and the unstable system will depart from the converged base state. To that end, the computed base flow is perturbed at $t = t_u$ by adding random white noise with amplitude ϵ_R to the solution. When the small perturbation dynamics is dominated by the most unstable eigenmode of the flow, the residual curve $\epsilon_R(t)$ is linear and corresponds to the exponential growth rate μ_i^c and $\ln(\epsilon_R)$ should therefore show a linear trend whose slope matches μ_i^c until non-linear saturation sets in.

4.2. Numerical set-up

An incompressible Navier-Stokes flow case defined by a two-dimensional circular cylinder at $Re = DU_\infty/\nu = 100$ is used as an application example. The Direct Numerical Simulations (DNS) of the cylinder flow have been performed using a conservative Finite-Volume (FV) Immersed Boundary Method (IBM) [23, 24]. The cylinder has diameter D. The two-dimensional domain $\boldsymbol{x} = [x, y]^T$ has the extent $-16D \leq x \leq 25D$ in the streamwise direction and $-22D \leq y \leq 22D$ in the transverse direction, which matches the domain used by Barkley [25]; the centre of the cylinder is located at $(0, 0)$. The structured mesh contains 5.1×10^5 hexahedral cells, with smooth hyperbolic refinement towards the cylinder in both directions. Uniform inflow velocity U_∞ is imposed at the inlet, no-slip conditions are applied at the surface of the cylinder and the pressure is fixed at the remaining boundaries. The flow field is initialised at a uniform streamwise velocity. The Navier-Stokes equations are advanced in time using an explicit third-order Runge-Kutta method with CFL = 1; a global time-stepping approach is used, since we are interested in studying the global properties of the flow field in time. ESFD is used to compute the base solution.

For validation purposes, the system's transient behaviour and stability obtained from the DNS is compared with the results from global linear stability analysis [26]. The stability analysis is performed for the base flow obtained from the instantaneous converged solution of the ESFD simulation. A Galerkin projection of the linearised

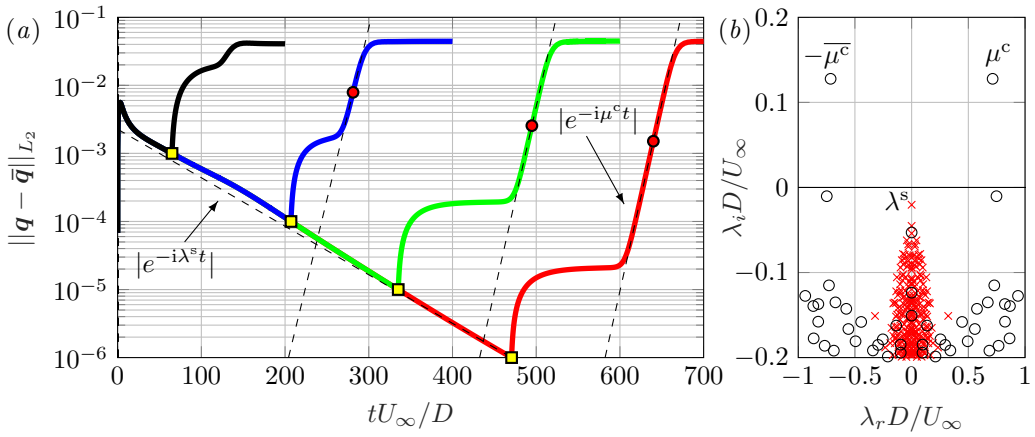

Figure 5: (a) SFD residual $\epsilon_{\mathrm{R}} = ||\boldsymbol{q}-\bar{\boldsymbol{q}}||_{L_2}$ (solid lines) using $\chi = 0.5$ and $\Delta = 3$. Fits to exponential parts (dashed lines). Unleash times (yellow squares) at $\epsilon_{\mathrm{R}} = 10^{-3}$ (black), 10^{-4} (blue), 10^{-5} (green), 10^{-6} (red). Location of null curvature in the linear range of the unleashed curves (red circles). (b) μ- (empty circles) and λ- (crosses) eigenspectrum from stability analysis computed with $\epsilon_{\mathrm{R}} = 10^{-6}$ base flow.

incompressible Navier-Stokes equations is performed to obtain an explicit discrete expression for the Jacobian $\boldsymbol{J}$ and to form the eigenvalue problem. The global eigenspectrum for the uncontrolled and controlled flow is respectively obtained as the eigenvalues of the matrices $-\mathrm{i}\boldsymbol{J}$ and $-\mathrm{i}\boldsymbol{G}$. The stability analysis is performed on the domain $-5D \leq x \leq 20D$, $-12.5D \leq y \leq 12.5D$. An unperturbed flow is assumed at both the cylinder, the inflow boundary and the transverse boundaries. A stress-free condition is prescribed at the outflow boundary. For the spatial discretisation, third-order C^0 multivariate spline elements [27, 28] are used to represent the velocity field. The pressure is eliminated from the equations by using a space of solenoidal velocity fields and a suitable choice of the variational formulation. Details regarding the numerical method are provided in [29].

4.3. Application to the cylinder flow

The results corresponding to four unleashed cases are shown in figure 5(a), using $\epsilon_{\mathrm{R}}(t_{\mathrm{u}} = 10^{-3}, 10^{-4}, 10^{-5}$, and 10^{-6}. The first main observation is that the expected linear growing trend of the residual curves starts developing after a significant number of time steps from the unleash. There is an initial transient after which the global mode develops. The exponential growth can be observed after all stable modes have died out. Regarding the range over which $\ln(\epsilon_{\mathrm{R}})$ grows linearly, two noteworthy considerations must be done. First of all, the point at which the linear growth starts developing depends on the amplitude of the noise imposed at $t = t_u$. However, the slope of the residual curves is independent of the initial disturbances, as expected. Secondly, the residual curves' slopes for the cylinder flow case are observed to increase asymptotically as ϵ_{R} decreases. From a physical point of view, throughout the controlled SFD simulation, the stabilised shear field must develop in time. Thus, for the present simulations, initialised with a uniform flow field, the growth rate of the associated Kelvin-Helmholtz (K-H) instability changes as the wake approaches the steady state. At a low enough residual level, the shear field can be assumed to be fully developed and μ^{c} approaches a limiting value. Following the same physical interpretation, the growth rate of the least stable eigenvalue of the controlled eigenspectrum, λ_i^{s}, changes throughout the controlled simulation. This may explain the slight bending of the residual curve of the SFD-stabilised simulation with respect to the expected linear behaviour for large ϵ_{R}, see figure 5(a). This is further discussed in §6.

The characterisation of μ^{c} requires to estimate the real part of μ^{c}. For that purpose, we suggest to compute the frequency from the time-signal measured with strategically placed probes. The probes are placed in areas where the eigenmode develops. This eigenmode associated to μ^{c} is represented in figure 6(b,d). The total measurement time is restricted to the linear growth phase. As pointed out by Barkley [25], the frequency of the eigenmode and the nonlinear limit cycle defer for non-critical Reynolds numbers. Therefore, the approach adopted by some authors, as for instance [8], to select Δ based on the frequencies captured in the fully developed non-linear flow is generally inadequate. When applying the flow unleash technique, the dominant frequency measured in the linear flow regime matches with the natural frequency of the unstable eigenmode developing in the flow, as shown in table 2.

To illustrate the accuracy of the flow unleash technique, table 2 compares μ^{c} obtained with this method, from stability analysis (using the $\boldsymbol{q}$ and $\bar{\boldsymbol{q}}$ fields as base flows) and with the value reported by Barkley [25]. One of the main advantages of the flow unleash technique is that the perturbation characterisation is carried out using

ϵ_R	**Flow unleash**	**Stability analysis (q)**	**Stability analysis ($\bar{q}$)**
10^{-3}	–	$\pm 0.7826 + 0.1426i$	$\pm 0.7873 + 0.1431i$
10^{-4}	$0.7240 + 0.1164i$	$\pm 0.7181 + 0.1287i$	$\pm 0.7183 + 0.1287i$
10^{-5}	$0.7139 + 0.1257i$	$\pm 0.7145 + 0.1278i$	$\pm 0.7145 + 0.1278i$
10^{-6}	$0.7135 + 0.1271i$	$\pm 0.7142 + 0.1277i$	$\pm 0.7142 + 0.1277i$

Table 2: $\mu^c D/U_\infty$ inferred using the flow unleash technique, global stability analysis using $\boldsymbol{q}$ or $\bar{\boldsymbol{q}}$ as the base flow at ϵ_R. Barkley [25] presents the value $\pm 0.7395 + 0.1298i$.

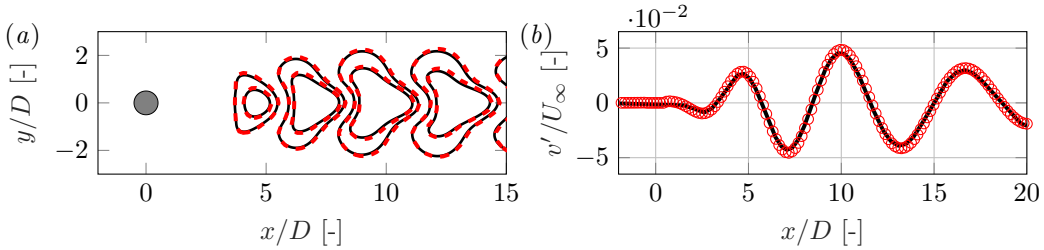

Figure 6: Dominant eigenmode (v') when the base flow is unleashed, associated to μ^c. (a) shows the xy-field, while (b) shows the profile along $y = 0$. Solid black lines: $\boldsymbol{q} - \bar{\boldsymbol{q}}$ from DNS, dashed red lines and red symbols: real part of global eigenfunctions from linear stability analysis.

the same numerical set-up as the flow simulation. Thus, the captured modal behaviour does correspond to the true perturbation dynamics in the simulation. On the other hand, when applying the flow unleash technique, the accuracy of the user-inferred eigenmode stability properties is subject to measurement errors. To minimise ambiguity, we propose to compute the value of $\mu_i^c = \partial \ln(\epsilon_R)/\partial t$ from the residual curves at the point of null curvature. The uncertainty of these measurements of μ_i^c for the present cylinder simulations is approximately $\pm 0.002\, U_\infty/D$. Here μ_r^c is determined as the average of the dominant frequency computed at probes placed at $(2, -1)$; $(2, 1)$; $(6, -1)$; $(6, 1)$. Table 2 also shows the convergence of μ^c with respect to ϵ_R when performing both stability analyses and DNS simulations, both methods match up to the measurement precision at $\epsilon_R = 10^{-6}$.

By keeping $\bar{\boldsymbol{q}}$ constant after the flow is unleashed, the field $\boldsymbol{q} - \bar{\boldsymbol{q}}$ becomes representative of the perturbation, $\boldsymbol{q'} = [u'\ v']^T$, developing in the unleashed flow field. This is valid under the assumption that $\bar{\boldsymbol{q}}(\boldsymbol{x}, t_u)$ sufficiently approximates $\boldsymbol{q}_s(\boldsymbol{x})$, which sets a requirement in the convergence level. Hence, the variable $\boldsymbol{q} - \bar{\boldsymbol{q}}$ can be compared to the eigenfunction of the unstable eigenmode developing in the unleashed flow field. Figure 6 shows that the mode ruling the flow unleash DNS matches the eigenmode of the stability analysis.

5. Optimisation

5.1. The role of stable eigenmodes

Jordi et al. [10] claim that the pair of χ and Δ that optimises the scalar problem (14) for μ^c also optimises the full flow problem. One result of §3.1 was that $\chi^\star$ and $\Delta^\star$ minimise the spectral radius of the scalar problem, since $\lambda^\star$ represents the configuration for which $\max\{\lambda_i(\mu^c)\}$ is located at the furthest possible distance from the real axis. Therefore, the application of the optimisation routine presented by Jordi et al. [10] and the expressions for $\chi^\star$ and $\Delta^\star$ are expected to yield the same convergence rate. To optimise the SFD set-up, however, the role played by the stable eigenvalues has to be considered as well, because the ultimate convergence rate of an SFD simulation is determined by the least stable eigenvalue λ^s, which does not necessarily correspond to $\lambda_{1,2}^c = \lambda_{1,2}(\mu^c)$. This philosophy also underlies the recently proposed Newton-Krylov method by Citro et al. [30], taking advantage of accounting for the slower decaying modes. The location of the least stable eigenvalue λ^s of the controlled eigenspectrum depends on the associated μ^s eigenvalue and the choice of parameters of the model χ and Δ.

When the stable eigenvalues are considered in the optimisation process, the choice $\chi^\star$ and $\Delta^\star$ leads to a suboptimal convergence rate, shown as follows. By combining the real part of the first expression with the imaginary part of second expression in eq. (20), we obtain

$$\lambda_{2,r}\left(\lambda_{1,i} + \frac{1}{\Delta}\right) + \lambda_{1,r}\left(\lambda_{2,i} + \frac{1}{\Delta}\right) = 0. \tag{42}$$

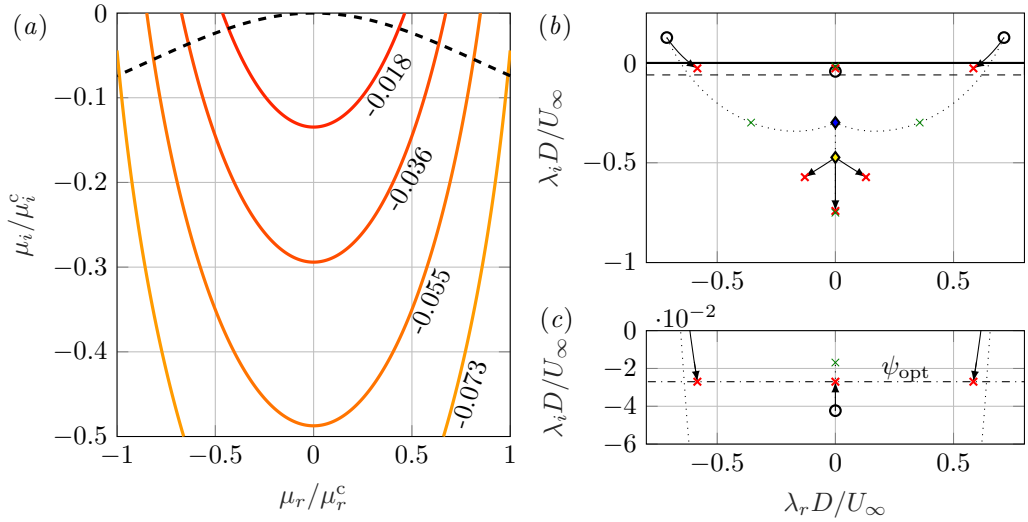

Figure 7: (a) Least stable λ_i isocontours (solid lines) in the μ space with $\chi = \chi^\star(\mu^c)$ and $\Delta = \Delta^\star(\mu^c)$ considering $\mu^c = 1 + 1\text{i}$. Boundary for which $\max\{\lambda_{1,i}, \lambda_{2,i}\} \lesseqgtr \mu_i$ (dashed line). (b) Path of λ-solutions varying χ in the range $[0, \chi_{\text{opt}}]$ with $\Delta = \Delta_{\text{opt}}$ (solid black arrows) and χ in the range $[0, \chi^\star]$ with $\Delta = \Delta^\star$ (dotted lines). (c) Zoom. μ (empty circles), $-\text{i}/\Delta_{\text{opt}}$ (yellow diamond), $-\text{i}/\Delta^\star$ (blue diamond), λ for $(\chi, \Delta) = (\chi_{\text{opt}}, \Delta_{\text{opt}})$ (red thick crosses), and λ for $(\chi, \Delta) = (\chi^\star, \Delta^\star)$ (green thin crosses).

Hence, for a fixed μ and variable χ and Δ, either one λ solution is located above $-\text{i}/\Delta$ and the complementary solution is located below $-\text{i}/\Delta$, or both solutions cross in imaginary part at $\lambda_{1,i} = \lambda_{2,i} = -1/\Delta$. The latter can only occur if [4]

$$\mu_i - \chi + \frac{1}{\Delta} = 0. \tag{43}$$

For a general eigenspectrum with many $\mu \neq \mu^c$, eq. (42) implies that the choice $\chi = \chi^\star(\mu^c)$ and $\Delta = \Delta^\star(\mu^c)$ places the solutions of each pair $\lambda_{1,2} \neq \lambda_{1,2}^c$ above and below $\lambda^\star(\mu^c)$ respectively. For this particular parameter choice, eq. (43) yields $\mu_i^c - \chi^\star(\mu^c) + 1/\Delta^\star(\mu^c) = 0$; thus all eigenvalues with $\mu_i \neq \mu_i^c$ have $\lambda_{1,2}$ located above and below $\lambda_i = -1/\Delta$. The implication for the optimisation of the SFD set-up is that the choice $\chi^\star$ and $\Delta^\star$ entails the existence of λ solutions with $\lambda_i > \lambda_i^\star$. The optimisation of the scalar problem thus generally implies suboptimal convergence of the full flow problem, since its application does not guarantee the minimisation of $\lambda_i^s > \lambda_i^\star$.

Next, a new hypothetical optimal configuration is proposed. To illustrate the role of χ and Δ in the $\mu \mapsto \lambda$ mapping, Åkervik et al. [4, figure 2] consider μ on the horizontal straight line, i.e., $\mu = \mu_r + b\text{i}$, $b \in \mathbb{R}$. Here, the analysis is restricted to $b < 0$, characterising stable eigenvalues. All μ are mapped onto two solution branches, one of them giving the least stable λ eigenvalue depending on the relation between b, χ and Δ. The μ's located close to the imaginary axis will be shifted upwards the most, the maximum being attained at $\mu_r = 0$. For a given full μ spectrum, the least stable λ^s may be associated to either the steady eigenvalue with the largest growth rate or less stable unsteady eigenvalues depending on their relative location on the complex plane and the parameters χ and Δ. Figure 7(a) is representative of this, illustrating that the largest λ_i correspond to μ located close to the imaginary axis.

When the previous analysis is extended to a general flow problem with discrete μ, the candidates to take the role of λ^s are stable, steady (or low-frequency) eigenmodes. It is unlikely for μ^c to take the role of λ^s, because the steady and low-frequency stable eigenvalues will be shifted upwards, while μ^c shifts downwards. The spectral radius is hypothetically minimised when the least stable λ solutions intersect $\max\{\lambda_{1,i}^c, \lambda_{2,i}^c\}$ in the imaginary coordinate at the furthest possible downwards distance from $\lambda_i = 0$.

The μ value corresponding to λ^s is denoted by μ^s and can be characterised by measuring the slope of the controlled SFD residual curve. This slope is proportional to λ_i^s and the frequency of the dominant wave-like perturbations in the controlled flow field corresponds to λ_r^s. Using the inverse mapping eq. (7), the value of μ^s can be determined.

For the cylinder flow case, the least stable μ that rules effective SFD simulations corresponds to a steady mode. That is, in the range of χ and Δ values that stabilises μ^c. For this reason, we assume μ^s to be purely imaginary in the analysis in the following section. By evaluating the slope of the SFD residual curve at $\epsilon_R = 10^{-6}$, it is obtained that $\mu^s D/U_\infty = -0.0423\text{i}$. The optimal configuration of the λ eigenvalues is illustrated in figures 7(b) and

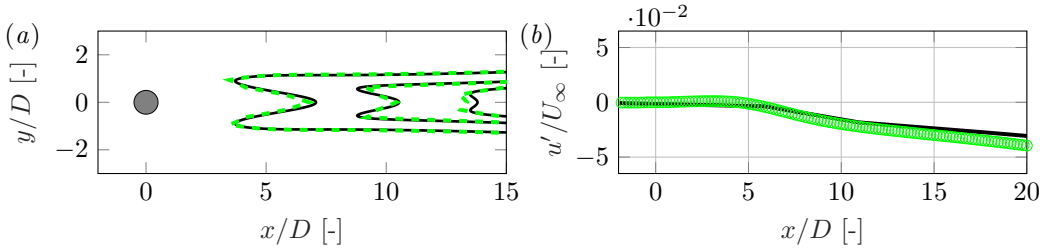

Figure 8: Dominant eigenmode of the flow (u') when applying SFD, associated to λ^{s}. (a) shows the xy-field, while (b) shows the profile along $y = 0$. Solid black lines: $\boldsymbol{q} - \bar{\boldsymbol{q}}$ from DNS, dashed green lines and green symbols: real part of global eigenfunctions from linear stability analysis.

(c). The arrows indicate the path followed by the selected μ when χ is increased from 0 at a fixed Δ. The final χ and Δ ($\chi_{\mathrm{opt}}, \Delta_{\mathrm{opt}}$), have been computed by using the method that we describe in §5.2. The artificial λ solutions emanating from the point located at $-\mathrm{i}/\Delta_{\mathrm{opt}}$ are far from becoming the least stable eigenvalues of the controlled eigenspectrum in this case. The natural λ solutions corresponding to μ^{c} and μ^{s} define the minimal spectral radius and cross in their imaginary part when $\chi = \chi_{\mathrm{opt}}$ and $\Delta = \Delta_{\mathrm{opt}}$. Note that the crossing in the imaginary part can take place for different combinations of χ and Δ. Within this set, χ_{opt} and Δ_{opt} correspond to the absolute minimum spectral radius.

In the linear controlled perturbation regime, the field $\boldsymbol{q} - \bar{\boldsymbol{q}}$ closely resembles the eigenfunction associated to λ^{s} obtained through an independent stability analysis, see figure 8, which yields $\mu^{\mathrm{s}} D/U_\infty = -0.0529\mathrm{i}$. Although the eigenvalue deviates from the growth measured from the slope of the SFD residual curve, the shape of the fields yield a convincing match. The main difference is observed close to the outflow boundary, and steady modes are indeed sensitively affected by boundary conditions.

5.2. Computation of optimal χ and Δ

The optimisation method presented next relies on running a controlled SFD or ESFD simulation and unleashing the flow afterwards. From the residual curves of the unleashed and controlled flow simulations, μ^{c} and μ^{s} can be inferred following the approaches described in §4 and §5.1, respectively. We define $\psi \in \mathbb{R}$ as the imaginary coordinate at which the vertical crossing of the λ's corresponding to μ^{c} and μ^{s} occurs. By operating on eq. (20), the minimal ψ

$$\psi_{\mathrm{opt}} = \frac{\mu_i^{\mathrm{s}}}{2 - \frac{(\mu_r^{\mathrm{c}})^2}{2\mu_i^{\mathrm{s}}\left(\mu_i^{\mathrm{s}} - \mu_i^{\mathrm{c}}\right)}} \left(\frac{\mu_i^{\mathrm{c}}}{\mu_i^{\mathrm{s}}} - \frac{(\mu_r^{\mathrm{c}})^2}{2\mu_i^{\mathrm{s}}\left(\mu_i^{\mathrm{s}} - \mu_i^{\mathrm{c}}\right)} + \frac{|\mu^{\mathrm{c}}|}{|\mu^{\mathrm{s}}|} \right). \tag{44}$$

is obtained for

$$\Delta_{\mathrm{opt}} = \frac{\mu_i^{\mathrm{s}}}{\psi_{\mathrm{opt}} \left(\frac{(\mu_r^{\mathrm{c}})^2}{2\left(\mu_i^{\mathrm{s}} - \mu_i^{\mathrm{c}}\right)} \left(\frac{\psi_{\mathrm{opt}}}{\mu_i^{\mathrm{s}}} - 1 \right) - \psi_{\mathrm{opt}} - \mu_i^{\mathrm{s}} + \mu_i^{\mathrm{c}} \right)}, \tag{45}$$

$$\chi_{\mathrm{opt}} = -\frac{1}{\Delta_{\mathrm{opt}}} - \psi_{\mathrm{opt}} + \mu_i^{\mathrm{s}} \left(1 + \frac{1}{\psi_{\mathrm{opt}} \Delta_{\mathrm{opt}}} \right). \tag{46}$$

In deriving these formulas, it is assumed that $\mu^{\mathrm{s}} = \mathrm{i}\mu_i^{\mathrm{s}}$, i.e., the controlled simulation is ruled by the critical steady eigenmode.

The residual curves corresponding to different model parameters are compared in figure 9. The spectral radius obtained with χ_{opt} and Δ_{opt} is 0.9734. This value closely resembles the optimal one of 0.979 reported by Cunha et al. [6], obtained through DMD. Following eq. (16), the optimal spectral radius presented in this article corresponds to $\lambda_i^{\mathrm{s}} D/U_\infty = -0.0270$; the spectral radius obtained by Cunha et al. [6] is given by $\lambda_i^{\mathrm{s}} D/U_\infty = -0.021$. A similar convergence rate is obtained using the analytical expressions with μ^{c} and μ^{s} either inferred from the controlled and unleashed residual curves or those obtained with the stability analysis. The first case appears to yield a slightly lower computational time, which means that the eigenvalues inferred through the application of the flow unleash technique are more representative for the dynamics in the simulation than the stability analysis. This may be related to the sensitivity of the stable steady mode to the outflow boundary conditions, as mentioned before. The stability analysis provides the full spectrum. We can thus verify that the found control parameters yield the optimal spectral radius accounting for the full eigenspectrum. No other eigenmode becomes dominant in this particular

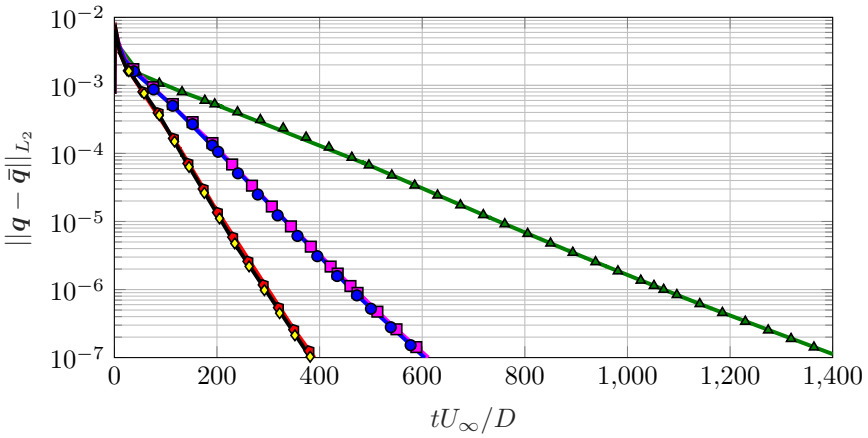

Figure 9: Comparison of the L_2 norm of $\boldsymbol{q}-\bar{\boldsymbol{q}}$ along ESFD simulations performed using different SFD parameters. The values of χ and Δ considered for each simulation are: $\chi_{\text{opt}} = 0.2524$ and $\Delta_{\text{opt}} = 2.1173$, optimal values computed by inferring μ^{c} and μ^{s} through the application of the technique of flow unleash (solid black line and yellow diamonds); $\chi_{\text{sp}} = 0.2608$ and $\Delta_{\text{sp}} = 2.1524$, optimal values computed with a previous knowledge of uncontrolled eigenspectrum (solid red line and red pentagons); $\chi^\star = 0.4259$ and $\Delta^\star = 3.3465$ (solid magenta line and magenta squares); $\chi = 0.4510$ and $\Delta = 3.1440$, reported by Jordi et al. [10] (solid blue line and blue circles); $\chi = 1$ and $\Delta = 5$ (solid green line and green triangles). All values of χ and $1/\Delta$ are given in units of U_∞/D.

case. The usage of $\chi^\star(\mu^{\text{c}})$ and $\Delta^\star(\mu^{\text{c}})$, which is suboptimal, yields the same performance as the parameters used by Jordi et al. [10], a result which is in agreement with the analysis exposed in §5.1. The optimised configuration reduces the computational time by 35%. A much larger reduction by 75% is observed when comparing χ_{opt} and Δ_{opt} and general SFD parameters, $\chi = 1$ and $\Delta = 5$. At $t \approx 400 U_\infty/D$, the usage of χ_{opt} and Δ_{opt} has converged the base flow to a residual level one order of magnitude lower than with the values presented by Jordi et al. [10] and three orders of magnitude lower than the usage of $\chi = 1$ and $\Delta = 5$.

6. Energy budget of the critical stable steady mode

The SFD simulations are ruled by a natural steady mode, which, obstructs the method from performing more efficiently. Despite the influence of the particular choice of the outflow boundary conditions, the latter arguments justify taking a closer look into the underlying physical mechanism which this mode represents. To that end, the Reynolds-Orr equation for $\tilde{\boldsymbol{q}}$ is considered:

$$\lambda = -\mathrm{i} \iint \left(u_s\, \tilde{\boldsymbol{q}}^* \cdot \frac{\partial \tilde{\boldsymbol{q}}}{\partial x} + v_s\, \tilde{\boldsymbol{q}}^* \cdot \frac{\partial \tilde{\boldsymbol{q}}}{\partial y} \right) \frac{\mathrm{d}x\,\mathrm{d}y}{||\tilde{\boldsymbol{q}}||^2} - D + R - \mathrm{i}\chi \frac{\tilde{\boldsymbol{q}}^* \cdot (\tilde{\boldsymbol{q}} - \tilde{\bar{\boldsymbol{q}}})}{||\tilde{\boldsymbol{q}}||^2} \tag{47}$$

where, in this case, $\tilde{\boldsymbol{q}} = [\tilde{u}\ \tilde{v}]^T$, $\tilde{\bar{\boldsymbol{q}}} = [\tilde{\bar{u}}\ \tilde{\bar{v}}]^T$, $\boldsymbol{q_s} = [u_s\ v_s]^T$, and $||\tilde{\boldsymbol{q}}||^2 = \iint \tilde{\boldsymbol{q}}^* \cdot \tilde{\boldsymbol{q}}\, \mathrm{d}x\,\mathrm{d}y$, see [3] for more details. From left to right, the terms represent advection, viscous dissipation D, Reynolds stress work R, and the SFD model terms, where:

$$D = \frac{\mathrm{i}}{Re} \iint \left(\left|\frac{\partial \tilde{u}}{\partial x}\right|^2 + \left|\frac{\partial \tilde{u}}{\partial y}\right|^2 + \left|\frac{\partial \tilde{v}}{\partial x}\right|^2 + \left|\frac{\partial \tilde{v}}{\partial y}\right|^2 \right) \frac{\mathrm{d}x\,\mathrm{d}y}{||\tilde{\boldsymbol{q}}||^2},$$

$$R = -\,\mathrm{i} \iint \left(|\tilde{u}|^2 \frac{\partial u_s}{\partial x} + \tilde{u}^* \tilde{v} \frac{\partial u_s}{\partial y} + \tilde{v}^* \tilde{u} \frac{\partial v_s}{\partial x} + |\tilde{v}|^2 \frac{\partial v_s}{\partial y} \right) \frac{\mathrm{d}x\,\mathrm{d}y}{||\tilde{\boldsymbol{q}}||^2}.$$

Given the set-up of the stability problem, no boundary contributions appear in this form of the expression.

By substituting the real-valued, steady mode solution, corresponding to the optimal SFD parameters into eq. (47), we obtain the budget shown in figure 10. Together, the bars add up to the value of λ_i, indicated with the dashed line. Due to the fact that the eigenfunction shapes in the SFD approach are only globally phase shifted versions of the shapes that would be encountered in the uncontrolled problem, eq. (9), dropping the bars associated to the SFD terms yields the μ_i-balance.

The term $-u_s\, \tilde{u}^* \partial \tilde{u}/\partial x$ is the largest in the budget. It has a stabilising effect, because $\tilde{u}$ increases in magnitude in the streamwise direction, see figure 6(a). This is a typical manifestation of the mechanism by which perturbation

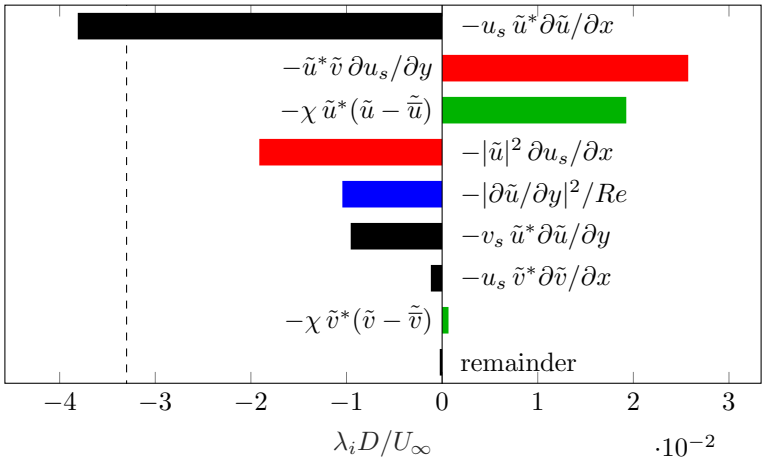

Figure 10: λ_i-budget (bars, $\iint \mathrm{Re}(\ldots)\mathrm{d}x\,\mathrm{d}y/||\tilde{\boldsymbol{q}}||^2$ of indicated terms) of the steady mode for the optimal control parameters $(\chi_{\mathrm{opt}}, \Delta_{\mathrm{opt}})$ according to equation eq. (47), λ_i eigenvalue (dashed line). Reynolds stress, viscous dissipation, advection and SFD model terms are coloured red, blue, black and green, respectively.

energy leaves the domain. The Reynolds stress $-\tilde{u}^*\tilde{v}\,\partial u_s/\partial y$ is the only destabilising term associated to the uncontrolled mode. This explains that, as the shear layers develop, this natural mode displays a decreasing decay rate, as is reflected in the residual curve in figure 5(a). Effectively, through these two main terms, this mode describes how the shear layers form (steadily) in the base flow in an uncontrolled simulation, the changes being washed out of the domain.

The action of SFD is to significantly decelerate this process through the term $-\chi\,\tilde{u}^*(\tilde{u}-\tilde{\bar{u}})$, having a magnitude comparable to the productive Reynolds stress. The balance furthermore features the normal Reynolds stress $-|\tilde{u}|^2\,\partial u_s/\partial x$, that is destructive as a consequence of the streamwise acceleration of the base flow. All other significant terms are stabilising, except for the SFD model term $-\chi\,\tilde{v}^*(\tilde{v}-\tilde{\bar{v}})$, but it has a very small relative size.

The model terms appear as $\mathrm{i}\,\tilde{\bar{\boldsymbol{q}}}^*\cdot(\tilde{\boldsymbol{q}}-\tilde{\bar{\boldsymbol{q}}})/\Delta = \lambda\tilde{\bar{\boldsymbol{q}}}^*\cdot\tilde{\bar{\boldsymbol{q}}}$ in the Reynolds-Orr equation for $\tilde{\bar{\boldsymbol{q}}}$ (dropping the integrals), meaning this term is directly responsible for forcing $\bar{\boldsymbol{q}}$ to the steady state, while a smaller proportional amount of energy is fed to the $\tilde{\boldsymbol{q}}$ budget; using eq. (9) the proportionality constant in this case is:

$$\chi_{\mathrm{opt}}\Delta_{\mathrm{opt}}\frac{\tilde{\boldsymbol{q}}^*\cdot(\tilde{\boldsymbol{q}}-\tilde{\bar{\boldsymbol{q}}})}{\tilde{\bar{\boldsymbol{q}}}^*\cdot(\tilde{\boldsymbol{q}}-\tilde{\bar{\boldsymbol{q}}})} = \frac{\chi_{\mathrm{opt}}\Delta_{\mathrm{opt}}}{\beta_1} = 0.5039, \tag{48}$$

where β_1 is used because the mode under investigation is the natural equivalent. So, the change in $\bar{\boldsymbol{q}}$ is transferred to $\boldsymbol{q}$ with the relative amplitude $\chi_{\mathrm{opt}}\Delta_{\mathrm{opt}}/\beta_1$, and then the dynamics of the $\boldsymbol{q}$ field acts to wash this out of the domain. The positivity of this constant implies that the $\bar{\boldsymbol{q}}$ solution is closer to $\boldsymbol{q}_s$ than $\boldsymbol{q}$ and its value is a measure of the difference.

7. Conclusions

We scrutinised the effect of the model parameters χ and Δ on the effectiveness and efficiency of Selective Frequency Damping (SFD). We proved that SFD is always able to stabilise systems that are unstable to one mode with a non-zero eigenfrequency. Simple expressions for the model parameters are presented, denoted by $\chi^\star$ and $\Delta^\star$, that are always able to quench an unsteady eigenmode and hence always succeed in driving the system towards the steady state.

These functionals were derived from the structure of the equations ruling the dynamics of SFD systems, whose simplified expressions are used to generate other relevant results, such as the demonstration that SFD is not capable of stabilising systems unstable to steady eigenmodes. Two different, but interconnected, behaviours of the λ eigenvalues of the controlled system are identified. We proved that choosing too large χ yields unstable behaviour of the controlled system, as opposed to what is indicated by Åkervik et al. [4]. We found that the SFD equations are self-similar to the argument of the unstable eigenvalue of the uncontrolled system and that the non-dimensional parameter $\mu_i^{\mathrm{c}}/\mu_r^{\mathrm{c}}$ (the ratio of the growth rate over the frequency of the most unstable eigenvalue μ^{c}) rules the

numerical feasibility of SFD. The larger μ_i^c/μ_r^c, the larger is the required relative accuracy of $\chi^\star$ and $\Delta^\star$ for the successful stabilisation of the system. Accordingly, depending on the digital precision of the numerical tools used to compute the base state, a threshold can be set for which the application of SFD is practically infeasible.

The stabilisation of systems unstable to more than one mode is challenging and can even be impossible depending on the dynamical characteristics of the system. Difficulties arise when unstable eigenvalues with large μ_i/μ_r are located close to the origin of the complex plane. We derived a simple analytical expression that can be used to determine whether SFD is capable of driving the system, unstable to multiple modes, towards the base solution. Under these conditions, a technique is introduced to select adequate χ and Δ yielding global stabilisation of the system.

The choice $\chi^\star$ and $\Delta^\star$ generally yields suboptimal performance in terms of convergence rate. Based on the dynamics of the controlled eigenvalues λ, we proposed a new hypothetical optimal configuration that leads to more efficient parameters than the current consensus established by Jordi et al. [10]. The optimisation analysis was based on the fact that the time-asymptotic SFD dynamics are governed by the least stable controlled eigenvalue λ^s; in the linear perturbation regime the spectral radius of the simulation is determined by λ_i^s.

We proposed the flow unleash technique for characterising the stability properties of the unstable eigenmode associated to the discretised system without having to perform an independent stability analysis. The technique relies on letting the small perturbation eigenmodes of the system develop on a sufficiently time-converged SFD base flow. From the controlled and flow unleash SFD simulations, the eigenvalues μ^s and μ^c ruling the dynamics of the stabilised and uncontrolled systems can be inferred. This allowed us to unequivocally determine the SFD parameters that minimise the spectral radius of the simulation, denoted by χ_{opt} and Δ_{opt}. Given the hypotheses that the base state is unstable to an unsteady discrete mode and the convergence of the stabilised dynamics is ruled by a stable steady mode, we presented analytical expressions for χ_{opt} and Δ_{opt}. By applying the flow unleash technique to the cylinder case, matching eigenmode dynamics are obtained with the results of independent stability analyses performed for the same base flow. Following the parameter optimisation method presented in this article, we observe a significant improvement with respect to the most efficient χ and Δ reported by Jordi et al. [10].

References

[1] H. L. Reed, W. S. Saric, D. Arnal, Linear stability theory applied to boundary layers, Annu. Rev. Fluid. Mech. 28 (1996) 389–428.
[2] V. Theofilis, Advances in global linear instability analysis of nonparallel and three-dimensional flows, Prog. Aerosp. Sci. 39 (2003) 249–315.
[3] P. J. Schmid, D. S. Henningson, Stability and Transition in Shear Flows, Springer, 2001.
[4] E. Åkervik, L. Brandth, D. S. Henningson, J. Hœpffner, O. Marxen, P. Schlatter, Steady solutions of the Navier-Stokes equations by selective frequency damping, Phys. Fluids 18 (2006) 357–397.
[5] D. A. Knoll, D. E. Keyes, Jacobian-free Newton-Krylov methods: a survey of approaches and applications, J. Comput. Phys. 193 (2004) 357–397.
[6] G. Cunha, P.-Y. Passaggia, M. Lazareff, Optimization of the selective frequency damping parameters using model reduction, Phys. Fluids 27 (2015) 094103.
[7] R. S. Teixeira, L. S. B. Alves, Minimal gain marching schemes: searching for unstable steady-states with unsteady solvers, Theor. Comput. Fluid Dyn. 31 (2017) 607–621.
[8] F. Richez, M. Leguille, O. Marquet, Selective frequency damping method for steady RANS solutions of turbulent separated flows around an airfoil at stall, Comput. Fluids 132 (2016) 51–61.
[9] B. E. Jordi, C. J. Cotter, S. J. Sherwin, Encapsulated formulation of the selective frequency damping method, Phys. Fluids 26 (2014) 034101.
[10] B. E. Jordi, C. J. Cotter, S. J. Sherwin, An adaptive selective frequency damping method, Phys. Fluids 27 (2015) 094104.
[11] E. Åkervik, J. Hœpffner, U. Ehrenstein, D. S. Henningson, Optimal growth, model reduction and control in a separated boundary-layer flow using global eigenmodes, J. Fluid Mech. 579 (2007) 305–314.
[12] B. Pier, Local and global instabilities in the wake of a sphere, J. Fluid Mech. 603 (2008) 39–61.
[13] P. J. Schmid, Global modes and control in a square cavity, AIAA Paper 2008-4229 (2008).
[14] S. Bagheri, P. Schlatter, P. J. Schmid, D. S. Henningson, Global stability of a jet in crossflow, J. Fluid Mech. 624 (2009) 33–44.
[15] A. Fani, S. Camarri, M. V. Salvetti, Unsteady asymmetric engulfment regime in a T-mixer, Phys. Fluids 26 (2014) 074101.
[16] J.-C. Loiseau, J.-C. Robinet, S. Cherubini, E. Leriche, Investigations of the roughness-induced transition: Global stability analyses and direct numerical simulations, J. Fluid Mech. 760 (2014) 175–211.
[17] H. B. E. Kurz, M. J. Kloker, Mechanisms of flow tripping by discrete roughness elements in a swept-wing boundary layer, J. Fluid Mech. 796 (2016) 158–194.
[18] E. Vyazmina, Bifurcations in a swirling flow, Ph.D. thesis, École Polytechnique X, 2010.
[19] L. E. Jones, R. D. Sandberg, Numerical analysis of tonal airfoil self-noise and acoustic feedback-loops, J. Sound Vib. 330 (2011) 6137–6152.
[20] L. Massa, Mach number effects on the global mixing modes induced by ramp injectors in supersonic flows, J. Fluid Mech. 757 (2014) 403–431.
[21] X. Garnaud, L. Lesshafft, P. J. Schmid, J.-M. Chomaz, A relaxation method for large eigenvalue problems, with an application to flow stability analysis, J. Comput. Phys. 231 (2012) 3912–3927.
[22] B. E. Jordi, Steady-state solvers for stability analysis of vortex dominated flows, Ph.D. thesis, Imperial College London, 2015.

[23] S. Hickel, C. Egerer, J. Larsson, Subgrid-scale modeling for implicit large eddy simulation of compressible flows and shock-turbulence interaction, Physics of Fluids 26 (2014) 106101.
[24] M. Meyer, A. Devesa, S. Hickel, X. Hu, N. Adams, A conservative immersed interface method for Large-Eddy Simulation of incompressible flows, J. Comput. Phys. 229 (2010) 6300–6317.
[25] D. Barkley, Linear analysis of the cylinder wake mean flow, Europhys. Lett. 75 (2006) 750–756.
[26] V. Theofilis, Global linear instability, Annu. Rev. Fluid. Mech. 43 (2011) 319–352.
[27] C. de Boor, B-form basics, in: G. E. Farin (Ed.), Geometric Modeling: Algorithms and New Trends, SIAM, Philadelphia, 1987, pp. 131–148.
[28] M. J. Lai, L. L. Schumaker, Spline functions on triangulations, volume 110 of *Encyclopedia of Mathematics and Its Applications*, Cambridge University Press, Cambridge, UK, 2007.
[29] H. J. Tol, M. Kotsonis, C. C. de Visser, Localised estimation and control of linear instabilities in 2-D wall-bounded shear flows, J. Fluid Mech. 824 (2016) 818–865.
[30] V. Citro, P. Luchini, F. Giannetti, F. Auteri, Efficient stabilization and acceleration of numerical simulation of fluid flows by residual recombination, Journal of Computational Physics 344 (2017) 234–246.